

Plasmonic Interactions through Chemical Bonds of Surface Ligands on PbSe Nanocrystals

Aloysius A. Gunawan,[†] Boris D. Chernomordik,[†] Dayne S. Plemmons,^{†,‡} Donna D. Deng,[†] Eray S. Aydil,[†] and K. Andre Mkhoyan*,[†]

[†]Department of Chemical Engineering and Materials Science, University of Minnesota, Minneapolis, Minnesota 55455, United States

[‡]Department of Chemical and Biomolecular Engineering, North Carolina State University, Raleigh, North Carolina 27695, United States

Supporting Information

ABSTRACT: When functional films are cast from colloidal dispersions of semiconductor nanocrystals, the length and structure of the ligands capping their surfaces determine the electronic coupling between the nanocrystals. Long chain oleic acid ligands on the surface of IV–VI semiconductor nanocrystals such as PbSe are typically considered to be insulating. Consequently, these ligands are either removed or replaced with short ones to bring the nanocrystals closer to each other for increased electronic coupling. Herein, using high-angle annular dark-field scanning transmission electron microscopy imaging combined with electron energy loss spectroscopy, we show that partial oxidation of PbSe nanocrystals forms conjugated double bonds within the oleic ligands, which then facilitates enhanced plasmonic interaction among the nanocrystals. The changes in the geometric configurations of the ligands are imaged directly and correlated with the changes in the surface plasmon intensities as they oxidize and undergo structural modifications.

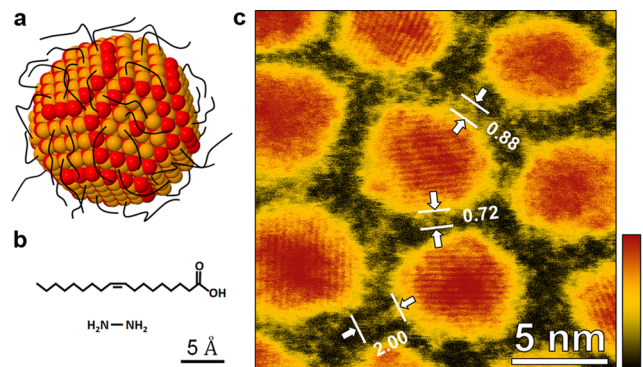
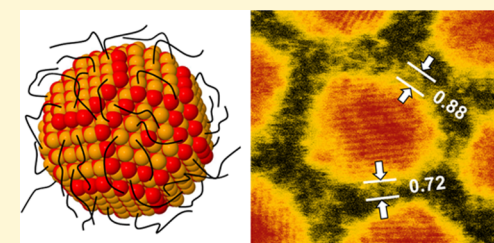


Figure 1. Geometric arrangements of the oleic acid ligands. (a) Schematic representation of the as-synthesized PbSe nanocrystal with oleic acid ligands. (b) Chemical structures of oleic acid and hydrazine molecules. (c) Atomic-resolution HAADF-STEM image of PbSe nanocrystals suspended on a ~5 nm thick a:Si TEM grids. Atomic planes along different crystallographic directions are visible for majority of the nanocrystals. The oleic acid ligands are attached to nanocrystals and extend to less than 1 nm radially from the surface of the nanocrystals. Indicated dimensions are in nanometers.

Colloidal semiconductor nanocrystals are the building blocks for a variety of optoelectronic devices including photodetectors,¹ light-emitting diodes,² sensors,³ and solar cells.⁴ Commonly used synthesis methods produce nanocrystals with surfaces capped with organic ligands. These ligands stabilize the colloidal dispersions of the nanocrystals and often electronically passivate the defects on their surfaces.⁵ The ligands are particularly important when the nanocrystal size is so small that their surface-to-volume ratio is large and electrons and holes are quantum confined within the periodic atomic lattice of the semiconductor.⁶ Consequently, the ligands on semiconductor nanocrystal surfaces play a critical role in determining their individual, as well as collective, electronic and optical properties. A technologically important example is lead salt (e.g., PbSe and PbS) nanocrystals, which have been used widely in quantum dot solar cells and infrared detectors.^{1–4} Films cast from dispersions of as-synthesized PbSe nanocrystals are insulating because the nanocrystals are capped with long oleate ligands that form a shell around the nanocrystals (Figure 1) and keep them too far apart from each other for facile charge transport. The oleate ligands are often removed with hydrazine,⁷ or replaced with shorter ligands such as ethanedithiol⁸ or pyridine⁹ to decrease the distance between the nanocrystals and to improve electronic coupling between the neighboring nanocrystals.¹⁰ This ligand-exchange approach results in enhanced electrical conduction in thin nanocrystal films¹¹ without loss of quantum confinement and enables novel solar cells that produce multiple electron–hole pairs per absorbed photon.⁴ The latter is attributed to multiple exciton generation (MEG) and leads to greater than 100% external quantum yields

in solar cells.¹² Interestingly, although simple description of the MEG suggests that the process should be independent of the choice of ligands,¹³ there is significant evidence that nano-

Received: April 9, 2014

Revised: May 1, 2014

Published: May 2, 2014



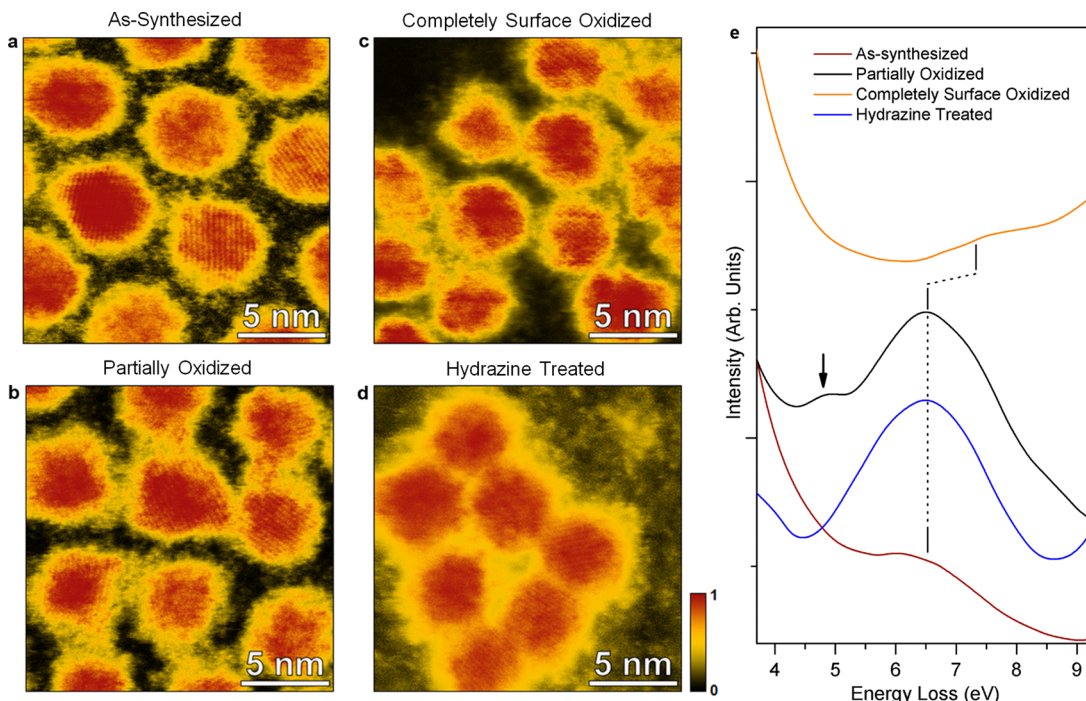


Figure 2. Atomic-resolution HAADF-STEM images and low-loss EELS of PbSe nanocrystals at different stages of oxidation. (a) As-synthesized, (b) partially oxidized, and (c) completely surface oxidized PbSe nanocrystals. Changes in ligands and reduction of nanocrystal size are visible as oxidation progresses. In the completely surface oxidized samples, the STEM probe beam first passes through the oxide shells on the outer surface resulting in additional spreading of the probe and hence the observed blurriness. (d) HAADF-STEM images of PbSe nanocrystals after hydrazine treatment. In hydrazine-treated samples, the oleic acid ligands were removed and nanocrystals are structurally modified. The residuals of the hydrazine treatment can be seen on a:Si substrate. (e) Low-loss EELS measurements from oleic acid-capped PbSe nanocrystal at different stages of oxidation and when the ligands treated with hydrazine. The spectra are vertically shifted for clarity. Narrowing of the LSPR EELS peak at 6.5 eV at the early stage of oxidation is seen. After complete surface oxidation, the LSPR EELS peak shifts to 7.5 eV. When nanocrystals are partially oxidized, an additional peak due to π -plasmons at 4.5 eV (arrow) is also detected.

crystal–ligand interactions and ligand-mediated internanocrystal electronic coupling affect the MEG efficiency,¹⁴ with most reports demonstrating high MEG efficiency in PbSe nanocrystals when short ligands are used.^{4,15}

The importance of the ligands attached to PbSe nanocrystals has motivated various studies of their structural properties. A variety of different techniques such as photoluminescence (PL), nuclear magnetic resonance (NMR), and molecular dynamics simulations were used to understand the bonding, stability, and geometric arrangements of these ligands on the PbSe nanocrystal surfaces.^{16–19} Direct imaging of ligands has only been reported for a few cases; citrate-capped Au nanocrystals and dodecene-octadecene-capped Si nanocrystals.^{20,21} Transmission electron microscopy (TEM) operated in scanning mode (STEM) with $\sim 1\text{--}2 \text{ \AA}$ electron probe is capable of such molecular scale imaging. Moreover, STEM equipped with an electron energy loss spectrometer (EELS) can be used to simultaneously image and probe the electronic coupling between nanocrystals when this coupling manifests itself as changes in the localized surface plasmon resonance (LSPR) within the nanocrystals. Such STEM-EELS studies have been reported for ligand-free Au and Ag metallic nanocrystals where high free electron densities allow probing of LSPR modes.^{22,23}

Herein, we show direct imaging of oleic acid ligands attached to the surface of semiconductor PbSe nanocrystals and observe chemical reactions within the ligands that lead to enhanced coupling between the nanocrystals. Specifically, the oleic acid ligands undergo oxidative dehydrogenation initiated by oxide layers on the nanocrystal surfaces. This chemical reaction leads to

enhanced coupling between the nanocrystals and facilitates surface plasmon interactions. Comparisons of oleic-acid-capped oxidized PbSe nanocrystals with hydrazine-treated nanocrystals verify this conclusion.

RESULTS AND DISCUSSION

The geometric arrangements of surface ligands were studied previously using molecular dynamics simulations of ligands bound to Pb atoms on perfectly faceted PbSe nanocrystals. These studies suggested that, generally, the ligands prefer to wrap around the surface when the number of the ligands is small. The same simulations showed that the ligands might stand in a more upright configuration (45° off the normal to the surface) when the Pb atom density on the facet is large and the configuration space is limited.¹⁸ The ratio of upright and wrapped ligands is determined by the balance between the van der Waals forces that tend to wrap the ligand around the surface and the entropic forces that tend to straighten the chains. This prediction is consistent with our experimental observations. Thickness and composition sensitive high-angle annular dark field STEM (HAADF-STEM) images of 6 nm as-synthesized PbSe nanocrystals (Figure 1) cast on thin a:Si TEM grids show that the oleic acid ligands form a corona around the nanocrystal surface. Most of the ligands are confined to a region less than 1 nm from the surface. Only a small fraction of the ligands are stretched and extend the entire length of the ligand, $\sim 2 \text{ nm}$, indicating that most of the ligands prefer conformations where the molecules stand at relatively small angles off the surface normal or lie against, and wrap around, the surface of the nanocrystals.

The appearance and structure of the oleate ligands on PbSe nanocrystals are function of the period of time the nanocrystals were exposed to air. Although it is well-known that PbSe nanocrystals oxidize when exposed to air, the changes in the ligands surrounding the nanocrystals have not been examined before. Oxidation of the PbSe nanocrystals blue shifts their photoluminescence spectrum²⁴ and changes the electronic conductivities of the nanocrystal films.²⁵ We examined the structural changes within the oleic acid ligands upon oxidation. We exposed the PbSe nanocrystals to air for different durations (see Methods) and examined their surfaces and interfaces with other PbSe nanocrystals. HAADF-STEM images show that upon oxidation, the region between the PbSe core and the oleate ligand corona becomes blurry and the diameter of the core decreases by approximately 1 nm (Figure 2). These changes are attributed to the formation of a self-limiting oxide shell on the nanocrystal surfaces.¹⁹ During the early stages, when surface oxidation is minimal, the ligands are more stretched than those on the as-synthesized nanocrystals resulting in the interdigititation of the ligands with ones on adjacent nanocrystals (Figure 2b).

To understand the effects of oxidation on the nanocrystals and ligands, we examined the nanocrystals with low energy loss EELS. The as-synthesized PbSe nanocrystals exhibit an EELS peak at 6.5 eV, which arises from the generation of LSPR in individual nanocrystals. The location of this peak agrees well with the frequency at which the Frölich condition is satisfied²⁶ (see the Supporting Information). During the early stages of oxidation, LSPR EELS peak narrows and its intensity increases significantly (Figure 2e), which suggests that the plasmon lifetime also increases. However, when surface oxidation is complete, the LSPR EELS peak broadens again. The decrease in the plasmon lifetime with surface oxidation is due to the oxide shell, which acts as an insulating barrier for the dephasing of the plasmons. When insulating oxide shells are formed, the conducting channels become blocked and hence the coupling of LSPR is suppressed. The blue shift of the peak to 7.5 eV is most likely due to changes in the size of nanocrystals after oxidation. The oxide shell has a smaller red-shift effect compared to the blue-shift due to the shrinking core size. However, the increase in the plasmon lifetime during the early stages of oxidation is unexpected. Because these low-loss EELS spectra were recorded under similar conditions (electron beam energy and dose), the observed changes in EELS cannot be electron beam induced.

A detailed core-level EELS study of the changes in bonding within the ligands during oxidation revealed the surprising reason for the plasmon lifetime increase. Figure 3 shows the carbon K-edge spectra collected from the oleic acid ligands on (i) as-synthesized, (ii) partially oxidized PbSe nanocrystals, and (iii) control bare oleic acid molecules not attached to nanocrystals. The spectrum from as-synthesized nanocrystals shows a π^* peak at 286 eV and a σ^* onset around 288.5 eV with relative intensities similar to those recorded from oleic acid molecules not attached to a nanocrystal (recorded from dried molecules deposited on a-Si TEM grid). Because EELS carbon K-edge spectra were recorded with same electron beam energy and similar beam doses, the results presented in Figure 3 also indicate that observed structural and electronic changes in ligands are not induced by electron beam, but inherent to oxidation of PbSe nanocrystals. The oleic acid molecule has 16 carbon–carbon σ bonds and 1 carbon–carbon π bond (see Figure 1b). In as-synthesized nanocrystals, the oleic acid ligands position, fold and wrap around the nanocrystals but do not undergo any dramatic

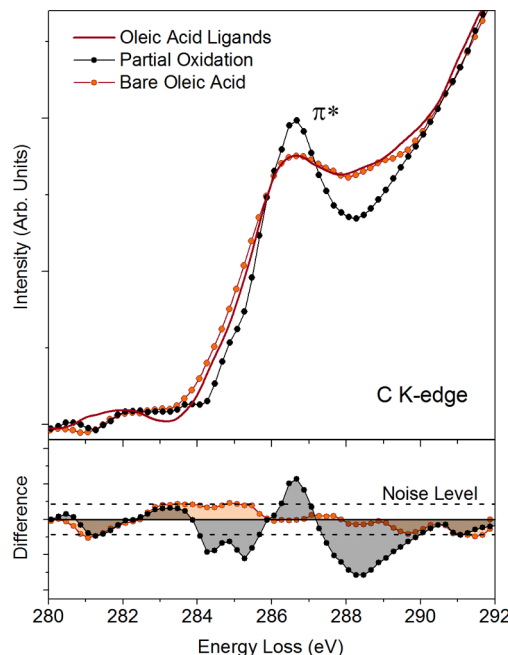


Figure 3. EELS carbon K-edges from ligands on PbSe nanocrystals before and after partial oxidation. Fine structures of the C K-edge recorded from oleic acid ligands when they are attached to the as-synthesized and partially oxidized PbSe nanocrystals. Spectrum from bare oleic acid molecules not attached to nanocrystals are also shown for comparison. Changes in π^* peak are visible. Differences with respect to the C K-edge spectrum from oleic acid ligands on as-synthesized PbSe nanocrystal are shown at the bottom. The noise levels are indicated by the dashed lines.

chemical changes when they are attached to the PbSe nanocrystals. However, changes in the internal bonds of the ligand are detected upon partial oxidation of the PbSe surface: specifically, the π^* peak increases, indicating the formation of new π bonds (see also the Supporting Information).

Additional evidence for appearance of new π bonds in the oleic acid ligands upon oxidation of the PbSe surface comes from the low-loss EELS (see Figure 2e). When the as-synthesized PbSe nanocrystals are partially oxidized, in addition to the LSPR peak at 6.5 eV, they also exhibit a weaker feature at 4.5 eV. This feature arises from the resonant oscillations of the delocalized π electrons, known as “ π -plasmons”. They are readily observed in graphene²⁷ and C₆₀.²⁸ Observation of π -plasmons and enhanced π^* loss at the carbon K-edge within oleic acid ligands is evidence for the formation of new π bonds. Moreover, the presence of π -plasmons indicates that these new π bonds are conjugated and their electrons are delocalized.

Formation of conjugated double bonds on carboxylic acids such as oleic acid typically occurs through oxidative dehydrogenation mechanism. Oxygen reacts with saturated carbon bonds in oleic acid to produce H₂O and form π bonds between the adjacent carbon atoms.²⁹ The presence of catalysts has been shown to reduce the activation energy for such dehydrogenation reaction.³⁰ In the case of partially oxidized PbSe nanocrystals, the oxygen on the surface of the nanocrystals can act as an initiator for the oxidative dehydrogenation. Specifically, we surmise that the oxidized PbSe surface provides the oxygen atoms to the ligands that are in close proximity of the surface as they wrap around the nanocrystal. As conjugated double bonds form, the ligands stiffen, straighten out, and interdigitate with the ligands on neighboring nanocrystals (Figure 4). In the absence of PbSe

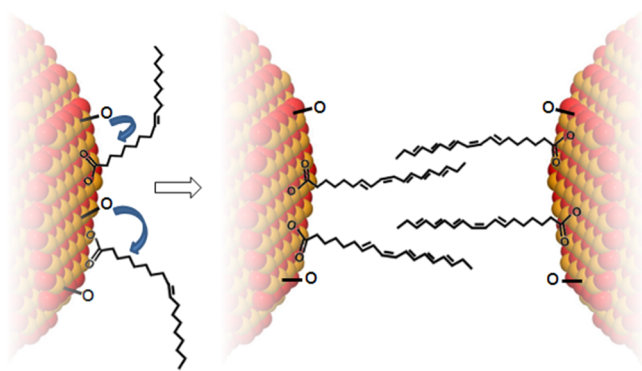


Figure 4. Schematic illustration of the changes in oleic acid ligands with oxidation. Oxidized PbSe nanocrystal acts as a catalyst for the wrapped ligands to undergo oxidative dehydrogenation by providing oxygen atoms. This dehydrogenation reaction with the formation of additional conjugated double bonds results in the disruption of the equilibrium wrapping arrangement and increase in the rigidity of the ligands facilitating interdigitation with neighboring ligands.

nanocrystals, there is no detectable oxidative dehydrogenation as evident from EELS data from bare oleic acid molecules cast on the same TEM grids: there are no significant changes in the π^* peak of the carbon K-edge in oleic acid molecules after they undergo similar oxidation treatment (see the Supporting Information).

As illustrated in Figure 5a, the oleic acid ligands on the as-synthesized nanocrystals passivate the dangling bonds of surface Pb atoms and introduce ligand states near the conduction band

edge.^{19,31} The HOMO level of the ligands accepts electrons from the nanocrystals and act as dephasing routes for surface plasmons (see Figure 5a). This dephasing is responsible for the broadening of the LSPR peak.³² This decay mechanism is often referred to as “chemical interface damping”. As the oxidation of the surface begins and surface oxygen facilitates the formation of conjugated ligands, conducting channels form between the nanocrystals. The conjugated ligands can support plasmonic interactions among the nanocrystals through charge transfer plasmons³³ (Figure 5b) and the plasmon decay mechanism via dephasing is removed. Consequently, the plasmon lifetime becomes longer, the LSPR peak narrows and the LSPR peak intensity in the low-loss EELS measurements increases (see Figure 2e). Similar LSPR peak narrowing and intensity enhancement with minimal red shift (<10 meV) have been observed previously when arrays of gold nanocrystals were brought closer together to induce electronic coupling.³⁴ We note that this charge transfer plasmon interaction is different from the more common dipolar interaction observed in metal nanocrystals at larger separation distances.³³

PbSe nanocrystals treated with hydrazine can be an excellent benchmark for evaluation of the surface plasmon lifetime and the LSPR peak, because hydrazine removes the oleic acid ligands and brings the nanocrystals as close to each other as possible (see Figures 2d and e). These touching nanocrystals have conducting channels between both the conduction bands and the valence bands of the neighboring nanocrystals through overlapping electronic wavefunctions (Figure 5c).¹⁰ Indeed, the LSPR excitations of the electrons in the conduction bands of the hydrazine-treated PbSe nanocrystals exhibit narrower and more

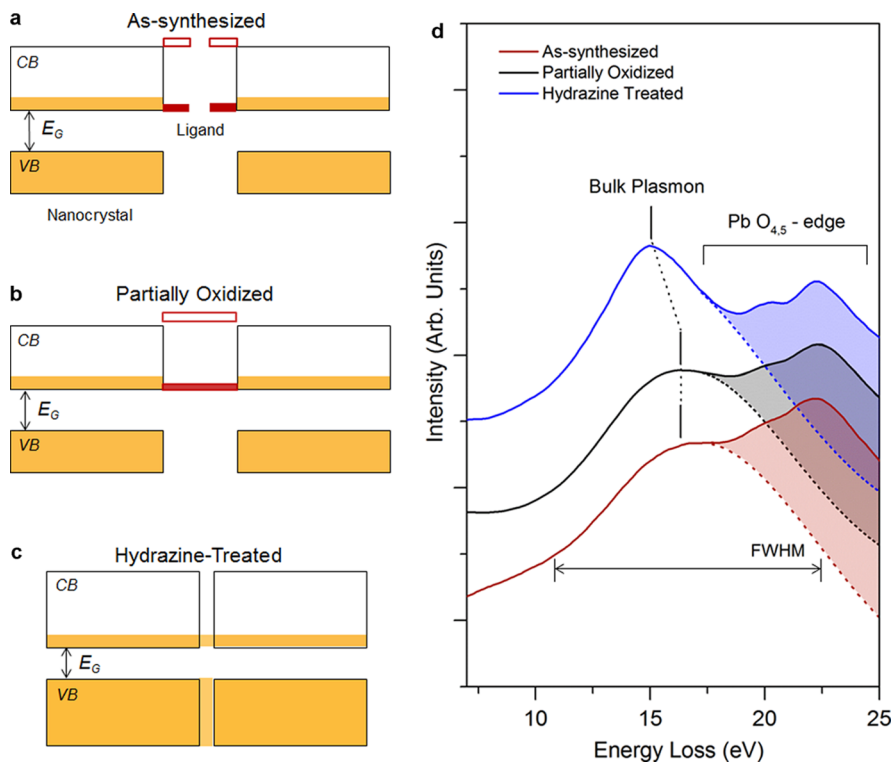


Figure 5. Schematic energy band diagrams for the PbSe nanocrystals and the ligands. (a) As-synthesized PbSe nanocrystal with oleic acid ligands, (b) partially oxidized PbSe nanocrystal with modified oleic acid ligands, and (c) nanocrystals after hydrazine treatment. (d) Low-loss EELS measurements from oleic acid-capped PbSe nanocrystal at different stages of oxidation and when nanocrystals are treated with hydrazine. The spectra are vertically shifted for clarity. The FWHM of the bulk plasmon EELS peak narrows from 11.5 eV for as-synthesized and partially oxidized nanocrystals with oleic acid ligands to 9 eV for nanocrystals when treated with hydrazine. The $\text{Pb O}_{4.5}$ -edge with onset at 17.5 eV is also detected in this EELS energy window.

intense LSPR peak than the LSPR of the as-synthesized and unoxidized PbSe nanocrystals. Remarkably, the intensities and widths of the LSPR peaks from hydrazine-treated and partially oxidized PbSe nanocrystals are very similar indicating similar plasmon lifetimes and coupling between the nanocrystals. This is despite the significant distance (~ 1.5 nm) between the partially oxidized nanocrystals, which are still covered with long and conjugated ligands. The important difference in the case of hydrazine-treated nanocrystals is the absence of the “ π -plasmon” peak at 4.5 eV. This is expected because interactions in hydrazine-treated nanocrystals are governed by their proximity to each other instead of conjugated carbon–carbon bonds of ligands as in partially oxidized nanocrystals.

The bulk plasmons, which originate from excitations of the valence band electrons, also exhibit the same behavior (Figure 5d). The bulk plasmon in as-synthesized PbSe nanocrystals appears at 16 eV with FWHM of 11.5 eV. This peak increases in intensity and narrows upon hydrazine treatment (FWHM = 9 eV). Such narrowing of bulk plasmon peaks has been observed in Si nanocrystals³⁵ and polycrystalline Au films.³⁶ The hydrazine treatment also red shifts the bulk plasmon peak to 15 eV, closer to the value for bulk PbSe (14.9 eV).³⁷ This shift is associated with the loss of quantum confinement as the individual nanocrystals electronically couple to each other.^{10,35} In ensembles of partially oxidized nanocrystals, coupling of the valence band electrons between neighboring nanocrystals is not expected (Figure 5b) and no changes should be observed in the FWHM of the bulk plasmon excitations. Indeed, our EELS measurements show that FWHM of the bulk plasmon signal from partially oxidized nanocrystals is practically the same as that from as-synthesized oleic acid capped PbSe nanocrystals (Figure 5d).

CONCLUSION

Using analytical HAADF-STEM, we have successfully imaged oleic acid ligands on PbSe nanocrystals and studied their chemical and conformational changes as the PbSe surface is oxidized. In as-synthesized nanocrystals, the ligands tend to wrap around the nanocrystal surface to maximize the nanocrystal core–ligand interaction. When exposed to atmosphere, PbSe nanocrystals begin to oxidize and the ligands undergo structural and chemical changes through oxidative dehydrogenation catalyzed by oxygen atoms on the nanocrystal surface. This oxidative dehydrogenation forms conjugated π bonds, which has profound effects on the electronic coupling between the nanocrystals. The π bonds stiffen the ligands enabling them to extend out and interdigitate with the ligands from neighboring nanocrystals. This provides enhanced electronic coupling between the nanocrystals. The effects of this coupling are detected with low-loss EELS measurements as enhanced plasmon lifetime and enhanced plasmon coupling between the nanocrystals.

MATERIALS AND METHODS

Materials. Selenium shot (Se, 99.999%) was purchased from Alfa Aesar. Anhydrous 200 proof ethanol (99.5%), anhydrous methanol (99.8%), anhydrous butanol (99.8%), anhydrous octane (99%), anhydrous hexane (99%), anhydrous acetonitrile (99.8%), trioctylphosphine (TOP, technical grade, 90%), oleic acid (technical grade, 90%), 1-octadecene (90%), lead(II) oxide (PbO, 99.999%), anhydrous hydrazine (98%), and diphenylphosphine (DPP, 98%) were purchased from Sigma-Aldrich.

Synthesis of Colloidal PbSe Nanocrystals. PbSe nanocrystal synthesis was based on the protocol developed by Murphy et al.⁵ and Luther et al.⁸ In a typical synthesis, PbO (2.5 g), oleic acid (9 mL), and 1-

octadecene (35 mL) were degassed three times on a Schlenk line at 40 °C and 15 mTorr, while stirring. The solution was then heated to 185 °C under N₂. A 1.00 M solution of selenium in trioctylphosphine (21 mL) and diphenylphosphine (0.3 mL), which was prepared inside an N₂-filled glovebox, was then swiftly injected. The solution turned black immediately. The temperature of the solution was maintained at 140–150 °C for 1 min. Then, 15 mL of ice-cold anhydrous octane was injected and the heat source was quickly replaced with an ice bath. The reaction mixture was extracted via cannula to a degassed Schlenk flask, which was then brought into the N₂-filled glovebox. The reaction mixture was then precipitated using anhydrous 200 proof ethanol via centrifuge and redispersed in anhydrous hexane, three times. The resulting particles were dispersed in hexane and stored in the glovebox. The size of the particles was determined from optical absorption of the colloidal dispersion using a published calibration curve in Moreels et al.³⁸

Preparation of Nanocrystal Films on TEM Grids. The as-synthesized PbSe nanocrystals were dispersed into hexane solution with 10 mg/mL concentration and dropcast onto TEM grids inside a glovebox. Nonporous amorphous Si from SIMPore, Inc. was used as the substrate for obtaining the images of oleic acid ligands and measuring LSPR and carbon K-edge signals. The substrates consist of nine windows of etched 3.5–5 nm thick a:Si sputter deposited on 100 μ m frames (see the Supporting Information). Ultrathin amorphous carbon (<5 nm) from Ted Pella, Inc. was used for acquiring bulk plasmon loss of the nanocrystal films since the bulk plasmon loss of the a:Si substrate at 17 eV, close to the bulk plasmon loss of PbSe.

Oxidation of Nanocrystals. The data from the as-synthesized samples were obtained from the freshly dropcast samples on TEM grids inside a glovebox that were transferred into TEM column without being exposed to air for more than 10 s. After collecting images and EELS data in TEM, these as-synthesized samples on TEM grids were stored in a low-humidity desiccator (24% RH). The samples were then re-examined with TEM at 5-day intervals. The signals from the partially oxidized samples were obtained after the third/fourth week. Samples typically become completely surface oxidized after 2 months.

Acquisitions of HAADF-STEM and EELS data. HAADF-STEM images and EELS spectra were acquired using FEI Tecnai G2 F30 S-TEM operated at 200 kV accelerating voltage and 60–300 mrad HAADF detector geometry. S-TEM is equipped with Gatan Enfinia-1000 spectrometer with 30 mrad collection angle. The energy resolution achieved for these experiments was 0.8–0.9 eV. Operating microscope at 200 keV, while is not the best condition for EELS, has advantage of improving high spatial resolution for HAADF-STEM imaging and minimizing possible radiolitic damage.³⁹ To avoid knock-on damage of the specimen (for both ligands and nanocrystals), the beam dose was dramatically reduced by recording EELS data in “area” mode at low magnifications. The area size used here was 20 \times 20 nm² with beam exposure time of 1 s for low-loss EELS and 5 to 8 s for core-level C K-edges. To improve signal-to-noise ratio of EELS, the data were recorded from 2-D or 3-D arrays of nanocrystals and two or three individual spectra were added. To ensure that recording HAADF-STEM images and EELS data are without significant contamination, we recorded ADF-STEM images before and after every critical EELS measurement or image acquisition and checked for signs of contamination. At the end, *B-spline* smoothing was applied to EELS data in Origin software for clarity.

Image Processing. The HAADF-STEM images were processed using contrast equalization algorithm performed in Digital Micrograph software to enhance the contrast of the surface ligands. The contrast equalization algorithm weights the intensity distribution of the ligands and nanocrystals using a nonlinear contrast instead of the customary linear contrast resulting in improved image contrast (see the Supporting Information). This was done only to improve the image representation in TIFF format. The actual image intensity from the surface ligands is above the noise level and quantifiable for one layer and multilayer ligands sticking on top of each other (see the Supporting Information).

■ ASSOCIATED CONTENT

Supporting Information

Details on samples, specimen preparation, STEM and EELS experiments, and data analysis. This material is available free of charge via the Internet at <http://pubs.acs.org>.

■ AUTHOR INFORMATION

Corresponding Author

*E-mail: mkhoyan@umn.edu. Tel: 612-625-2059. Fax: 612-626-7246.

Notes

The authors declare no competing financial interest.

■ ACKNOWLEDGMENTS

This work was supported partially by the MRSEC Program of the U.S. National Science Foundation (NSF) under Award DMR-0819885. Parts of this work were carried out in the Characterization Facility at the University of Minnesota, which receives partial support from NSF through the MRSEC program.

■ REFERENCES

- (1) Konstantatos, G.; Howard, I.; Fischer, A.; Hoogland, S.; Clifford, J.; Klem, E.; Levina, L.; Sargent, E. H. *Nature* **2006**, *442*, 180–183.
- (2) Sun, L.; Choi, J. J.; Stachnik, D.; Bartnik, A. C.; Hyun, B.-R.; Malliaras, G. G.; Hanrath, T.; Wise, F. W. *Nat. Nanotechnol.* **2012**, *7*, 369–373.
- (3) Somers, R. C.; Bawendi, M. G.; Nocera, D. G. *Chem. Soc. Rev.* **2007**, *36*, 579–591.
- (4) Semonin, O. E.; Luther, J. M.; Choi, S.; Chen, H.-Y.; Gao, J.; Nozik, A. J.; Beard, M. C. *Science* **2011**, *334*, 1530–1533.
- (5) Murphy, J. E.; Beard, M. C.; Nozik, A. J. *J. Phys. Chem. B* **2006**, *110*, 25455–25461.
- (6) Tang, J.; Kemp, K. W.; Hoogland, S.; Jeong, K. S.; Liu, H.; Levina, L.; Furukawa, M.; Wang, X.; Debnath, R.; Cha, D.; et al. *Nat. Mater.* **2011**, *10*, 765–771.
- (7) Law, M.; Luther, J. M.; Song, Q.; Hughes, B. K.; Perkins, C. L.; Nozik, A. J. *J. Am. Chem. Soc.* **2008**, *130*, 5974–5985.
- (8) Luther, J. M.; Law, M.; Song, Q.; Perkins, C. L.; Beard, M. C.; Nozik, A. J. *ACS Nano* **2008**, *2*, 271–280.
- (9) Hanrath, T.; Veldman, D.; Choi, J. J.; Christova, C. G.; Wienk, M. M.; Janssen, R. A. J. *ACS Appl. Mater. Interfaces* **2009**, *1*, 244–250.
- (10) Williams, K. J.; Tisdale, W. A.; Leschkies, K. S.; Haugstad, G.; Norris, D. J.; Aydil, E. S.; Zhu, X. Y. *ACS Nano* **2009**, *3*, 1532–1538.
- (11) Talapin, D. V.; Murray, C. B. *Science* **2005**, *310*, 86–89.
- (12) Ellingson, R. J.; Beard, M. C.; Johnson, J. C.; Yu, P.; Micic, O. I.; Nozik, A. J.; Shabaev, A.; Efros, A. L. *Nano Lett.* **2005**, *5*, 865–871.
- (13) Luther, J. M.; Beard, M. C.; Song, Q.; Law, M.; Ellingson, R. J.; Nozik, A. J. *Nano Lett.* **2007**, *7*, 1779–1784.
- (14) Beard, M. C.; Midgett, A. G.; Law, M.; Semonin, O. E.; Ellingson, R. J.; Nozik, A. J. *Nano Lett.* **2009**, *9*, 836–845.
- (15) Kim, S. J.; Kim, W. J.; Sahoo, Y.; Cartwright, A. N.; Prasad, P. N. *Appl. Phys. Lett.* **2008**, *92*, 031107–3.
- (16) Stouwdam, J. W.; Shan, J.; van Veggel, F. C. J. M.; Pattantyus-Abraham, A. G.; Young, J. F.; Raudsepp, M. *J. Phys. Chem. C* **2006**, *111*, 1086–1092.
- (17) Sapra, S.; Nanda, J.; Pietryga, J. M.; Hollingsworth, J. A.; Sarma, D. D. *J. Phys. Chem. B* **2006**, *110*, 15244–15250.
- (18) Kaushik, A. P.; Clancy, P. *J. Chem. Phys.* **2012**, *136*, 114702–12.
- (19) Moreels, I.; Fritzinger, B.; Martins, J. C.; Hens, Z. *J. Am. Chem. Soc.* **2008**, *130*, 15081–15086.
- (20) Lee, Z.; Jeon, K.-J.; Dato, A.; Erni, R.; Richardson, T. J.; Frenklach, M.; Radmilovic, V. *Nano Lett.* **2009**, *9*, 3365–3369.
- (21) Panthani, M. G.; Hessel, C. M.; Reid, D.; Casillas, G.; José-Yacamán, M.; Korgel, B. A. *J. Phys. Chem. C* **2012**, *116*, 22463–22468.
- (22) Chu, M.-W.; Myroshnychenko, V.; Chen, C. H.; Deng, J.-P.; Mou, C.-Y.; García de Abajo, F. J. *Nano Lett.* **2008**, *9*, 399–404.
- (23) Koh, A. L.; Bao, K.; Khan, I.; Smith, W. E.; Kothleitner, G.; Nordlander, P.; Maier, S. A.; McComb, D. W. *ACS Nano* **2009**, *3*, 3015–3022.
- (24) Sykora, M.; Koposov, A. Y.; McGuire, J. A.; Schulze, R. K.; Tretiak, O.; Pietryga, J. M.; Klimov, V. I. *ACS Nano* **2010**, *4*, 2021–2034.
- (25) Leschkies, K. S.; Kang, M. S.; Aydil, E. S.; Norris, D. J. *J. Phys. Chem. C* **2010**, *114*, 9988–9996.
- (26) Moreels, I.; Allan, G.; De Geyter, B.; Wirtz, L.; Delerue, C.; Hens, Z. *Phys. Rev. B* **2010**, *81*, 235319.
- (27) Eberlein, T.; Bangert, U.; Nair, R. R.; Jones, R.; Gass, M.; Bleloch, A. L.; Novoselov, K. S.; Geim, A.; Briddon, P. R. *Phys. Rev. B* **2008**, *77*, 233406.
- (28) Hunt, M. R. C.; Rudolf, P.; Modesti, S. *Phys. Rev. B* **1997**, *55*, 7889–7903.
- (29) Fukudome, K.; Ikenaga, N.-o.; Miyake, T.; Suzuki, T. *Catal. Sci. Technol.* **2011**, *1*, 987–998.
- (30) Botella, P.; García-González, E.; Dejoz, A.; López Nieto, J. M.; Vázquez, M. I.; González-Calbet, J. J. *Catal.* **2004**, *225*, 428–438.
- (31) Bryant, G. W.; Jaskolski, W. *J. Phys. Chem. B* **2005**, *109*, 19650–19656.
- (32) Anatoliy, P.; Uwe, K. *New J. Phys.* **2003**, *5*, 151.
- (33) Zuloaga, J.; Prodan, E.; Nordlander, P. *Nano Lett.* **2009**, *9*, 887–891.
- (34) Liljeroth, P.; Vanmaekelbergh, D.; Ruiz, V.; Kontturi, K.; Jiang, H.; Kauppinen, E.; Quinn, B. M. *J. Am. Chem. Soc.* **2004**, *126*, 7126–7132.
- (35) Mitome, M.; Yamazaki, Y.; Takagi, H.; Nakagiri, T. *J. Appl. Phys.* **1992**, *72*, 812–814.
- (36) Chen, K.-P.; Drachev, V. P.; Borneman, J. D.; Kildishev, A. V.; Shalaev, V. M. *Nano Lett.* **2010**, *10*, 916–922.
- (37) Büchner, U. *Phys. Status Solidi B* **1977**, *83*, 493–500.
- (38) Moreels, I.; Lambert, K.; De Muynck, D.; Vanhaecke, F.; Poelman, D.; Martins, J. C.; Allan, G.; Hens, Z. *Chem. Mater.* **2007**, *19*, 6101–6106.
- (39) Holmberg, V. C.; Helps, J. R.; Mkhoyan, K. A.; Norris, D. J. *Chem. Mater.* **2013**, *25*, 1332–1350.